

Article

# Multi-Step Ageing Prediction of NMC Lithium-Ion Batteries Based on Temperature Characteristics

**Abdelilah Hammou** , **Boubekeur Tala-Ighil**, **Philippe Makany** and **Hamid Gualous** \*

LUSAC Laboratory, University of Caen Normandy, 50130 Cherbourg-Octeville, France;  
abdelilah.hammou@unicaen.fr (A.H.)

\* Correspondence: hamid.gualous@unicaen.fr

**Abstract:** The performance of lithium-ion batteries depends strongly on their ageing state; therefore, the monitoring and the prediction of the battery state of health (SoH) is necessary for an optimized and secured functioning of battery systems. This paper evaluates and compares three artificial neural network architectures for multi-step ageing prediction of lithium-ion cells: Recurrent Neural Network (RNN), Gated Recurrent Unit (GRU) and Long short-term memory (LSTM). These models use the features extracted from the cell's temperature to predict the cell's capacity. The features are extracted from experimental measurements of the cell's surface temperature and selected based on Spearman correlation analysis. The prediction results were evaluated and compared considering three different percentages of the training dataset: 60%, 70%, and 80%. Training and testing data were generated experimentally based on accelerated ageing cycling tests. During these experiments, four Nickel Manganese Cobalt/Graphite (NMC) cells were cycled under a controlled temperature environment based on a dynamic current profile extracted from the Worldwide Harmonized Light Vehicles Test Cycles.

**Keywords:** lithium-ion batteries; ageing; prediction; state of health; artificial neural networks



**Citation:** Hammou, A.; Tala-Ighil, B.; Makany, P.; Gualous, H. Multi-Step Ageing Prediction of NMC Lithium-Ion Batteries Based on Temperature Characteristics. *Batteries* **2024**, *10*, 384. <https://doi.org/10.3390/batteries10110384>

Academic Editors: Xiaoyuan Shi and Hengguo Wang

Received: 20 September 2024

Revised: 21 October 2024

Accepted: 28 October 2024

Published: 31 October 2024



**Copyright:** © 2024 by the authors. Licensee MDPI, Basel, Switzerland. This article is an open access article distributed under the terms and conditions of the Creative Commons Attribution (CC BY) license (<https://creativecommons.org/licenses/by/4.0/>).

## 1. Introduction

Lithium-ion batteries present the main energy storage system used in transport applications [1,2], thanks to their greater advantages in comparison with other energy storage systems: high power and energy density, fast response time, and wide operating temperature range [3,4]. However, these characteristics depend strongly on the battery ageing stage [5,6]. The degradation of lithium-ion batteries generally leads to three degradation modes: the loss of lithium inventory, the loss of active material, and the increase in the internal resistance [7]. These ageing modes lead to the fade of the battery capacity and power [8]. Therefore, to ensure the proper functioning of the battery and to anticipate failure, several studies have been carried out to predict the battery capacity for its ageing prognosis [9]. The state-of-health prediction methods in the literature are classified in two categories: model-based methods and data-driven methods [10,11].

Model-based methods exploit mathematical/physical models of battery ageing to predict the future evolution of a battery's capacity. These models are first calibrated and fitted based on the historical data of battery capacity. The prediction is obtained by the extrapolation of the model to future cycles [12]. The main advantage of the model-based approaches is the ability to learn even when the available data are limited in quantity [13]. In [14], the authors combined the Particle Filter (PF) with the Genetic Algorithms (GA) for the prediction of the battery capacity; the modelling of the capacity fade is performed based on the multiphase sigmoidal model. The results evaluation showed that the Root Mean Squared Percentage Error (RMSPE) of the capacity prediction is less than 1.2% when the model is fitted based on 60% of cycles. In addition, the study in [15] used the Particle Swarm Optimization (PSO) for the prediction of the battery capacity based on the dual

exponential model, and the performance of PSO was enhanced by PF. The method was verified using two public datasets: NASA and CALSE datasets. Moreover, in [16] the authors combined two empirical models for the prediction of the battery capacity: the double-exponential model and the polynomial model; the aim of this combination is to enhance the adaptability of the perdition approach to different degradation trends. The model parameters are estimated using the PF. The evaluation of the proposed method confirms the accuracy of these methods in comparison with one single model.

Data-driven methods, on the other hand, are based on designing and fitting forecasting models based on the historical data to predict the battery ageing evolution [17]. The main advantage of these methods is their flexibility, since they are model-free approaches; consequently, they can be adapted to several scenarios and cycling conditions [18]. In [19], the authors combined a CNN-LSTM-Attention neural network with transfer learning for the capacity prediction; the input features of the proposed model were extracted using Complete Ensemble Empirical Mode Decomposition with Adaptive Noise (CEEDMAN). The experimental evaluation of the proposed approach shows that the Mean Absolute Percentage Error (*MAPE*) of the predictions is less than 2%. The study in [20] compared two deep LSTM network architectures for the prediction of the battery capacity: the one-step prediction architecture, and the multi-step prediction architecture. Furthermore, the work presented in [21] combines the Convolutional Neural Network (CNN) with the bidirectional LSTM neural network for the prediction of the battery capacity. The method was trained and tested based on two public datasets: NASA and CALCE. The Root Mean Squared Error (*RMSE*) of the prediction is less than 0.025 when the model is trained with 50% of cycles.

The discussed prognosis methods are interesting and presented accurate prediction results. However, in vehicular applications, the working conditions of batteries depend on driver behavior and also climatic conditions [22]. As a result, the ageing trajectory of the battery systems varies with the variation of working conditions [23]. Therefore, the prediction algorithms should be trained based on the historical data of each vehicle battery. Additionally, the computational power for embedded applications is limited; thus, the prediction algorithms should be less computationally intensive [24]. This paper presents and compares three variants of recurrent neural networks for multi-step prediction of battery capacity based on the cell's thermal behavior. The models' assessment aims to select the suitable method for vehicular conditions. The ageing data used for model training and testing were generated experimentally based on accelerated ageing tests of four NMC cells at controlled temperature. During these tests, the cells were cycled under a dynamic current profile extracted from the Worldwide Harmonized Light Vehicles Test Cycles (WLTC) [25]. Prediction results were analyzed and compared considering three percentages of the cell cycles in order to evaluate the prediction models against training size and cell ageing stage. The evaluation also takes into consideration the model accuracy and complexity.

The rest of the paper is organized as follows: Section 2 presents the experimental data used in this study and details the prediction structure and the prognosis models. Section 3 presents the prediction results and their analysis. A conclusion closes the paper.

## 2. Materials and Methods

### 2.1. Experimental Data

The experimental data used for model training and validation are obtained from accelerated cycling tests of four cells of Nickel Manganese Cobalt (NMC) at a controlled temperature of 35 °C [26]. The cells are charged using Constant-Current Constant Voltage mode (CC-CV) and then discharged using a dynamic current profile adapted from the Worldwide Harmonized Light Vehicles Test Cycles (WLTC) [25]. Figure 1 displays the current profile applied during the cycling process (charge and discharge). This cycling operation is repeated during five days, and then a check-up test is carried out to measure the cell's performance at 25 °C. The check-up tests aim to measure the battery capacity, energy, and direct current internal resistance (DCIR) [26].

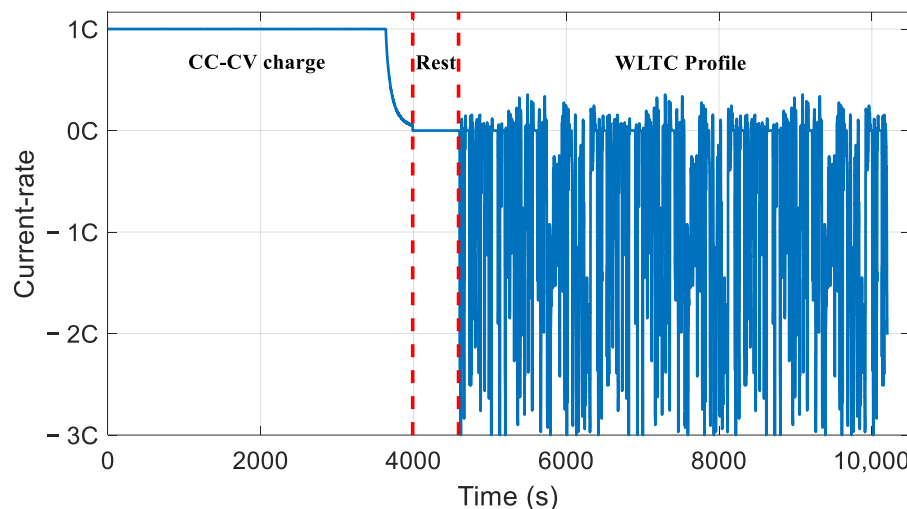


**Figure 1.** Applied current during cell cycling.

These experiments are carried out using a CHROMA 17020<sup>®</sup> battery tester (Chroma ATE Europe B.V., AH Ede, The Netherlands) that allows the cycling of eight cells at the same time. This device enables the acquisition of the charging/discharging current, the cell voltage and the cell surface temperature using a type T thermocouple. The temperature is conditioned using a Weiss Technik<sup>®</sup> climate chamber (Weiss Technik France S.A.S, Eragny, France). In these tests, four cells of Nickel Manganese Cobalt/Graphite (NMC) with a rated capacity of 3 Ah are cycled [27].

The temperature is measured at three points on the cell's surface: near the anode, near the cathode, and in the middle of the cell, as presented in Figure 2. The sampling period for data acquisition is set at  $T_s = 1$  s. Figure 3 shows the evolution of capacity as a function of the number of cycles for the four cells in each chemistry.

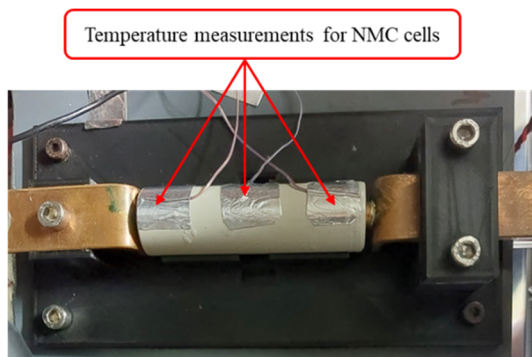


**Figure 2.** Temperature measurement points at the cell surface.

The experimental tests validate the effect of cycling on the loss of cell performance; the results show the fade of battery capacity and energy and the increase in the DCIR with cycles. The cell's capacity and energy decrease with 20% and 27%, respectively, while the DCIR growth is greater than 200%. The results also show that the energy decline is higher than the capacity decline; this difference is related to the dependence of the energy on both cell capacity and internal resistance.

The comparison between cells' ageing behavior reveals the variation of ageing evolution between cells, which is related to the cell's inconsistency [28]. Thus, prediction models should consider cell inconsistency for improving prediction results.

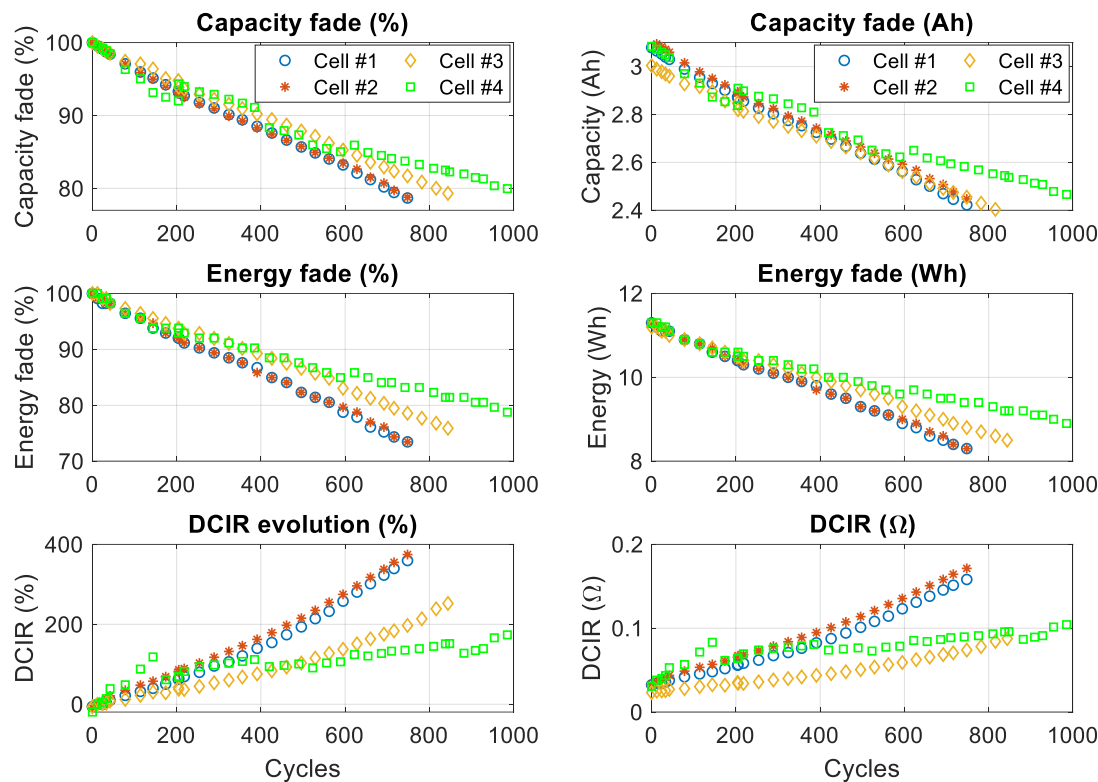


**Figure 3.** Cycling characterization results.

The generated experimental data allow for the extraction and the analysis of thermal features during battery discharging with the dynamic current profile, which allows the evaluation of the prediction models under conditions close to vehicular conditions. However, in order to design generalized prediction models, the future work will focus on the extension of the experimental tests to different temperatures and state-of-charge ranges.

## 2.2. Features Extraction

The cell ageing rate is highly dependent on the battery temperature, as reported in several studies [29], and at the same time the temperature behavior of a battery varies with ageing [30]. Therefore, exploring the temperature characteristics of the batteries will provide information about the battery SoH and rate. The experimental results presented in Figure 4 confirm the effect of ageing on the temperature behavior of the cells. The temperature measured on the cell surface shows that the cell's temperature increases with ageing; the maximum temperature reaches 38 °C at the beginning of the life, while it increases with 1 °C after 350 cycles; at the end of life, the temperature reaches 42 °C.

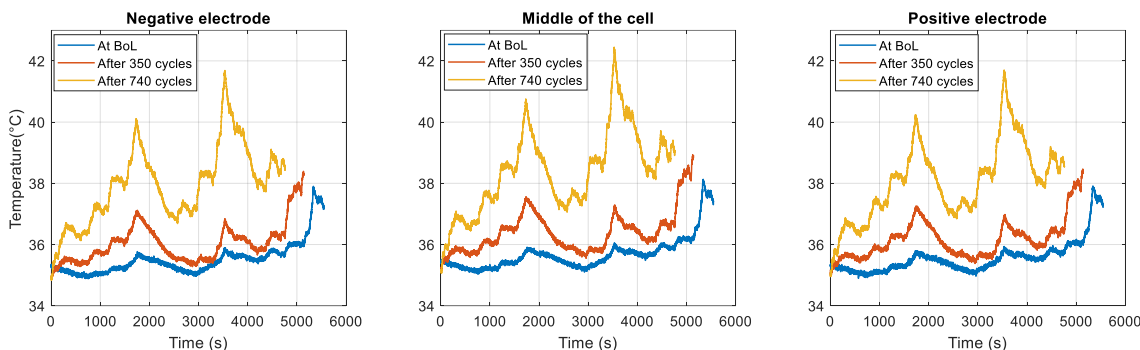


**Figure 4.** Temperature profile measured at the cell's surface at three different ageing stages.

In order to exploit the information contained in the temperature curves, several features are calculated from the cell's surface temperature during its discharging: the mean, the variance, and the maximum of the temperature curve under the WLTC profile. Figure 5 shows the evolution of the features extracted from temperature measurements as a function of cycles for one cell (Cell 1).

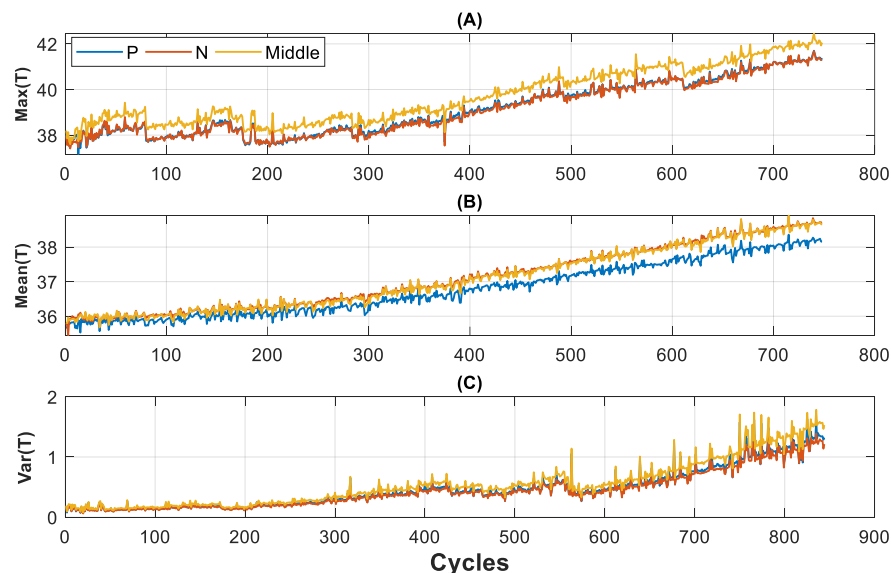


**Figure 5.** Evolution of the extracted features as a function of the performed cycles: (A) the evolution of the maximum temperature, (B) the evolution of the mean temperature, and (C) the evolution of the temperature variance.

The results obtained show that the extracted features increase with the cycles. The comparison between the temperatures at three different points on the surface of the cell shows that the three points present the same trends. In order to evaluate and analyze the correlation between the extracted features and the cell's SoH, the Spearman correlation is used to assess their correlation (Equation (1)). The Spearman correlation coefficient [31] evaluates the existence of a monotonic linear or non-linear relationship between two variables,  $X$  and  $Y$ . Figure 6 presents the heat map of the Spearman coefficient correlation between the extracted features and the cell capacity.

$$R_{Spearman} = 1 - \frac{6\sum_{i=1}^n d_i^2}{n^3 - n} \quad (1)$$

where  $n$  is the number of observations, and  $d_i$  is the difference between  $\text{rank}(X_i)$  and  $\text{rank}(Y_i)$ .

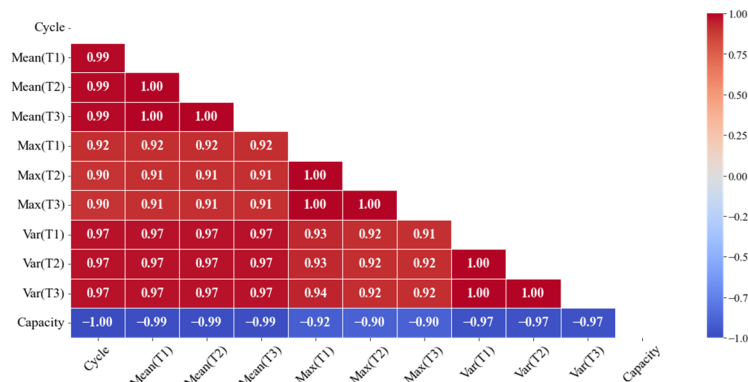


**Figure 6.** Heatmap of the Spearman coefficient correlation between the extracted features and the capacity for cell 1.

The analysis of the correlation results showed that the cycle number and the mean value of the surface temperature are the most correlated features with battery capacity; the Spearman coefficient correlation is greater than 0.99. In addition, based on the results in Figure 5, it is noted that the evolution of the mean value is more regular, unlike the maximum value and the variance, which present some fluctuations and disturbances. The comparison of the evolution of the means of the three measurement points shows that they have the same correlation coefficient and follow almost the same trend with the degradation (Figure 5). Therefore, to simplify the architecture of neural networks, instead of using the three temperature measurements, only the temperature measured in the middle of the cell will be used, since it is the least sensitive point to external temperature variation [32]. Consequently, the mean value of the temperature and the cycle number are used as inputs for the neural networks.

### 2.3. Prognosis Models

In this study, three variants of recurrent neural networks have been used for the prediction of the cell capacity: Recurrent Neural Network (RNN), Long Short-Term Memory (LSTM), and Gated Recurrent Unit network (GRU). The use of recurrent networks is related to their ability to handle time series data, as discussed in several studies [17–21,33], which is the case for this study, where the objective is to predict the temporal evolution of the cell's capacity. Figure 7 presents the architectures of the RNN, LSTM, and GRU units.

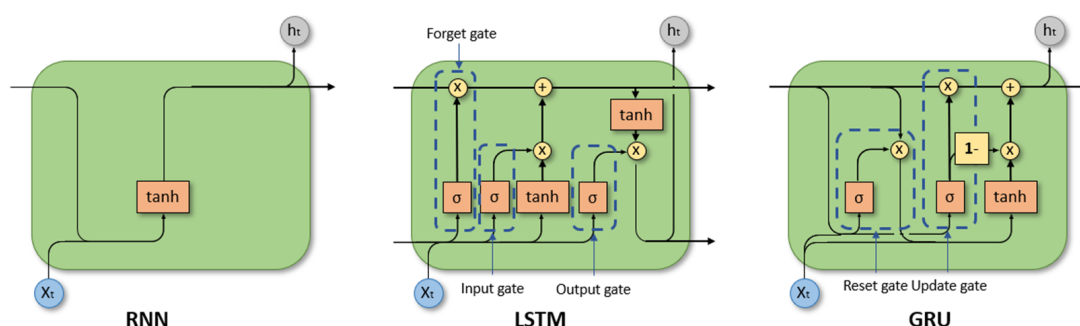


**Figure 7.** Architecture of RNN, LSTM, and GRU units [34].

#### (a) Recurrent Neural Networks

A Recurrent Neural Network (RNN) is designed to work with sequential data [35], such as word sequences or time series. In classical neural networks, inputs are processed independently of each other, whereas RNNs are able to take into account the history of the input data to predict the next output value. This is possible thanks to feedback loops that allow information to flow through the network and be stored in an internal memory called a hidden state. The hidden state of the RNN units,  $h_t$ , is updated based on the previous state  $h_{t-1}$  and the input at the time step  $t$  (Equation (2)):

$$h_t = \tanh(w_i[h_{t-1}, x_t] + b_h) \quad (2)$$

where  $w_i$  is the weight matrix,  $b_h$  is the bias vector, and  $\tanh$  is the hyperbolic tangent function. Therefore, the unit output is calculated based on the hidden state  $h_t$  (Equation (3)):

$$y_t = W_o * h_t + b_y \quad (3)$$

where  $W_o$  and  $b_y$  are the weight matrix and the bias vector, respectively. Table 1 summarizes the RNN configuration (architecture and hyperparameters) used for the multi-step capacity prediction.

**Table 1.** RNN neural network configuration and hyperparameters.

Parameter	Configurations
Input layer	300 RNN units
Hidden layer-1	200 RNN units
Hidden layer-2	100 RNN units
Output layer	Dense unit with Leaky Rectified Linear Unit activation function [36]
Optimizer	'ADAM' optimizer [37] with Mean Squared Error (MSE) as a loss function

### (b) Long Short-Term Memory

Long Short-Term Memory (LSTM) neural networks are a class of recurrent neural networks. They were introduced to solve the vanishing gradient problem in the back-propagation of traditional RNN [38]. LSTM takes into account long-term dependencies in temporal data by using an internal memory to store important contextual information. The LSTM architecture consists of three gates: the input gate, the forget gate, and the output gate described by equations (Equation (4)), (Equation (5)) and (Equation (6)), respectively [38]. These gates play a role in determining which data to keep and which to discard, which helps to keep only the relevant data, to facilitate prediction by the sequence chain.

$$i_t = \sigma(w_i[h_{t-1}, x_t] + b_i) \quad (4)$$

$$f_t = \sigma(w_f[h_{t-1}, x_t] + b_f) \quad (5)$$

$$o_t = \sigma(w_o[h_{t-1}, x_t] + b_o) \quad (6)$$

where  $w_X$  is the weight matrix,  $b_X$  the bias, and  $\sigma$  the sigmoid function for gate X. The candidate state cell  $\tilde{c}_k$  is calculated using (Equation (7)):

$$\tilde{c}_t = \tanh(w_c[h_{t-1}, x_t] + b_c) \quad (7)$$

where  $w_c$  and  $b_c$  are the weight and bias for the candidate state cell  $\tilde{c}_t$ , and  $\tanh$  is the hyperbolic tangent function.

Subsequently, the state cell  $c_t$  is updated based on the previous state  $c_{t-1}$  and the candidate state  $\tilde{c}_t$  (Equation (8)). The final output  $h_t$  is calculated using (Equation (9)).

$$c_t = f_t * c_{t-1} + i_t * \tilde{c}_t \quad (8)$$

$$h_t = o_t * \tanh(c_t) \quad (9)$$

Table 2 sums up the LSTM architecture and hyperparameters used for the multi-step capacity prediction.

**Table 2.** LSTM neural network configuration and hyperparameters.

Parameter	Configurations
Input layer	300 LSTM units
Hidden layer-1	200 LSTM units
Hidden layer-2	100 LSTM units
Output layer	Dense unit with Leaky Rectified Linear Unit activation function [36]
Optimizer	'ADAM' optimizer [37] with Mean Squared Error (MSE) as a loss function

### (c) Gated Recurrent Unit network

The Gated Recurrent Unit (GRU) network aims to keep the advantages of the gating mechanism in the LSTM unit while reducing the number of parameters, thus reducing the network complexity [39]. The GRU unit is composed of two gates: update and reset gates.

The update gate  $u_t$  evaluates the significance of the features in the time series and catches long-term dependencies. The reset gate  $r_t$  determines the amount of past information to be forgotten. The update and reset gates are calculated based on the current input vector  $x_t$  and the previous hidden state  $h_{t-1}$ , as described by the following equations (Equations (10) and (11)):

$$u_t = \sigma(w_u[h_{t-1}, x_t] + b_u) \quad (10)$$

$$r_t = \sigma(w_r[h_{t-1}, x_t] + b_r) \quad (11)$$

where  $w_u, w_r$  are the weight matrices of the update and reset gates,  $b_u$  and  $b_r$  are the biases, and  $\sigma$  denotes the sigmoid function. The candidate hidden state  $\tilde{h}_t$  can be expressed using (Equation (12)):

$$\tilde{h}_t = \tanh(w_h[r_t * h_{t-1}, x_t] + b_h) \quad (12)$$

where  $w_h$  and  $b_h$  are the weight matrix and bias of the candidate hidden state, respectively, and  $\tanh$  refers to the hyperbolic tangent function. Therefore, the current hidden state  $h_t$  is obtained based on the candidate state and the previous hidden state (Equation (13)):

$$h_t = (1 - u_t) * h_{t-1} + u_t * \tilde{h}_t \quad (13)$$

Table 3 sums up the GRU architecture and hyperparameters used for the capacity prediction.

**Table 3.** GRU neural network configurations and hyperparameters.

Parameter	Configurations
Input layer	100 GRU units
Hidden layer-1	50 GRU units
Hidden layer-2	25 GRU units
Output layer	Dense unit with Leaky Rectified Linear Unit activation function [36]
Optimizer	'ADAM' optimizer [37] with Mean Squared Error (MSE) as a loss function

(d) Parameter initialization and regularization

- He Initialization

The weights of the neural network models are initialized using the He initialization method [40]. The objective of this initialization is to provide an appropriate initialization of the weights that avoids the saturation and vanishing gradient problems during the training of the network.

The He initialization method takes into account the size of the previous layers when initializing the weights. The weights are initialized with a normal distribution centered on zero and a variance adapted to the size of the previous layer. More precisely, the weights are randomly drawn according to a normal distribution with a variance of  $2/N$ , where  $N$  represents the number of neurons in the previous layer. This initialization promotes a more efficient propagation of information through the network, by avoiding too low or too high values of the weights.

- L2 regularization

L2 regularization is a technique used in model training to prevent overfitting of neural network models [41]. It consists of penalizing high values of the model's weights, which allows controlling their relative importance during training.

In this case, the loss function is Mean Squared Error (MSE) [42] (Equation (14)):

$$L = \frac{1}{N_s} * \sum_{i=1}^{N_s} (\hat{Y}_i - Y_{exp})^2 \quad (14)$$

where  $N_s$  represents the number of samples,  $\hat{Y}_i$  represents the output of the model, and  $Y_{exp}$  is the actual value. The training process of the model consists of adjusting the model parameters (weights and biases) to minimize the loss function  $L$ .

L2 regularization consists of adding the following term to the cost function (Equation (15)) [41]:

$$L = \frac{1}{N_s} * \sum_{i=1}^{N_s} (\hat{X}_i - X_{exp})^2 + \lambda \sum_{i=1}^P w_i^2 \quad (15)$$

where  $w_i$  are the model weights and  $\lambda$  is the regularization parameter. L2 regularization adds a penalty term to the loss function that applies strong penalties to larger weights, which favors smaller ones.

### 3. Results

#### 3.1. Model Training and Evaluation

The neural network models are trained with three different percentages of data (60%, 70%, and 80% of data). This percentage refers to the ratio of the number of cycles used for model training to the number of cycles performed by the cells during their lifetime. This procedure allows the evaluation at different ageing stages of the cells and also considering different amounts of data.

The prediction errors are evaluated using the *MAPE* and the *RMSE* described by equations (Equation (16)) and (Equation (17)), respectively.

$$MAPE(\%) = 100 * \frac{1}{N} * \sum_1^N |\hat{X} - X_{exp}| / X_{exp} \quad (16)$$

$$RMSE(Ah) = \frac{1}{N} * \sqrt{\sum_1^N (\hat{X} - X_{exp})^2} \quad (17)$$

#### 3.2. Prediction Results and Discussion

With the aim to maximize the number of capacity values that can be predicted in one shot (multi-step prediction), Figure 8 presents the evolution of the average *MAPE* of all cells as a function of the prediction steps (the capacity values predicted simultaneously). These results are obtained when the neural network models are trained with 60% of cycles.

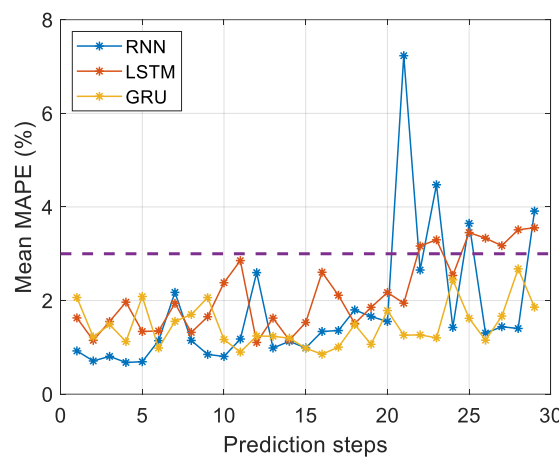


**Figure 8.** Evolution of the mean *MAPE* error as a function of the prediction steps for the three prognosis models (RNN, LSTM, and GRU).

The analysis of the evolution (Figure 8) of the prediction errors as a function of the predicted steps shows that the RNN model presents the lowest error when predicting five capacity values. However, as the number of predicted steps increases, the prediction errors of the three models are very close and stay lower than 3% until 20 predicted steps. When predicting more than 20 capacity values, the mean *MAPE* for the RNN reaches the value

of 7%, fluctuates and becomes unstable, pointing to its weakness to capture long-term dependencies due to its simple architecture [35]. Concerning the LSTM model, the *MAPE* continues to increase progressively with the cycles to exceed the value of 3%. The *MAPE* for the GRU model is always lower than 3%. Based on the LSTM and the GRU architectures discussed in Section 2.3, the LSTM model is expected to show high accuracy compared to the GRU model due to its gating mechanisms. However, the results show the opposite; this could be related to the insufficiency of the training data for the LSTM network, since the number of parameters to optimize for LSTM is higher than that of the GRU [43].

In order to compare and analyze the results of the three neural networks for each cell, the prediction steps are fixed at 20 in the rest of this study. Figures 9–11 present the prediction results of the three prediction models in comparison with the measured capacity, for the tree training set 60%, 70%, and 80%, respectively. Table 4 presents the calculation of the *MAPE* and the *RMSE* of the prediction results of the three prognosis models; the mean value of errors of the four cells is also calculated.

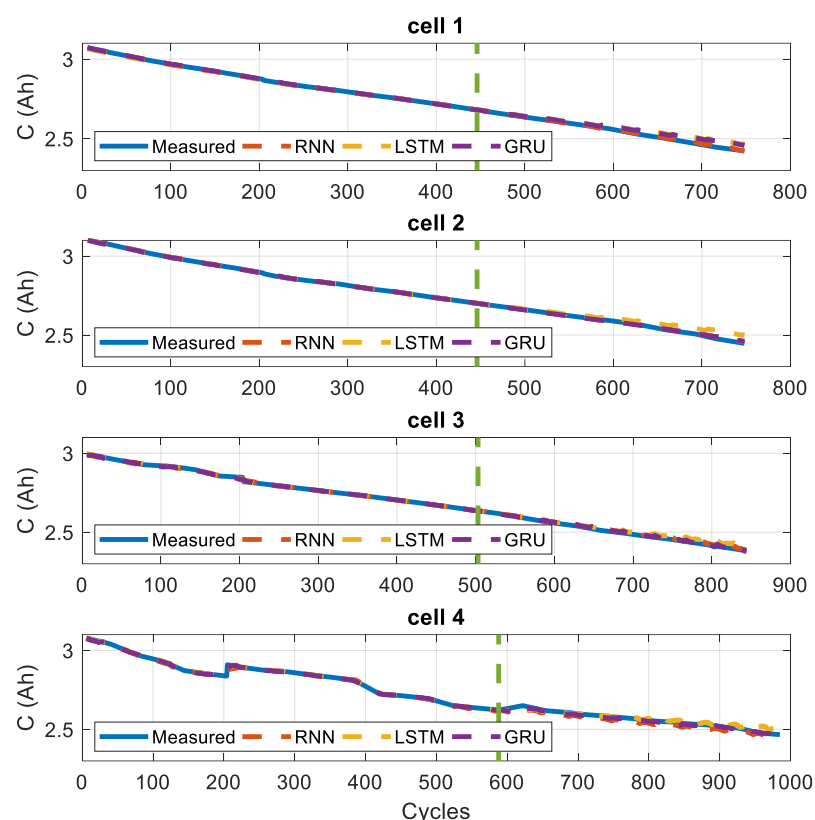


**Figure 9.** Prediction results of the three prognosis models in comparison with the measured capacity when the models are trained with 60% of the cycles.

The results obtained in Figures 9–11 show that the three prognosis models present an accurate prediction result for the three training percentages: the *MAPE* and the *RMSE* errors are less than 2.5% and 0.054 Ah, respectively, for the four cells.

The analysis of the evolution of the prediction accuracy (Table 4) shows that, for the three neural networks, the prediction accuracy increases with the increasing of training data: the increase in the percentage of the training cycles from 60% to 80% allowed the mean *MAPE* to be reduced from 2% to 5% for the RNN model, from 1.616% to 0.732% for the LSTM model, and from 1.183% to 0.169% for the GRU model. However, when comparing the error evolution for individual cells, the analysis shows that the error does not decrease with the training data increasing for all cells: for cells 1, 2 and 3, the results show that in some cases the error increases with the increase in training data. Concerning cell 4, the prediction accuracy increases with the increasing training set. This difference

can be related to the overfitting of the prediction models on the data of cells 1, 2 and 3, where the capacity evolution is quasi-linear in comparison with cell 4, where the evolution is nonlinear.

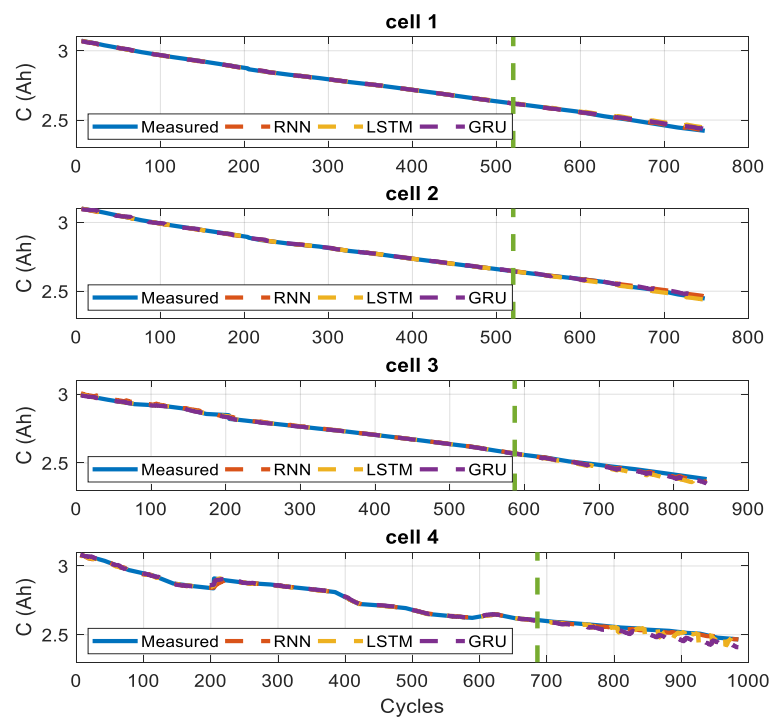


**Figure 10.** Prediction results of the three prognosis models in comparison with the measured capacity when the models are trained with 70% of the cycles.

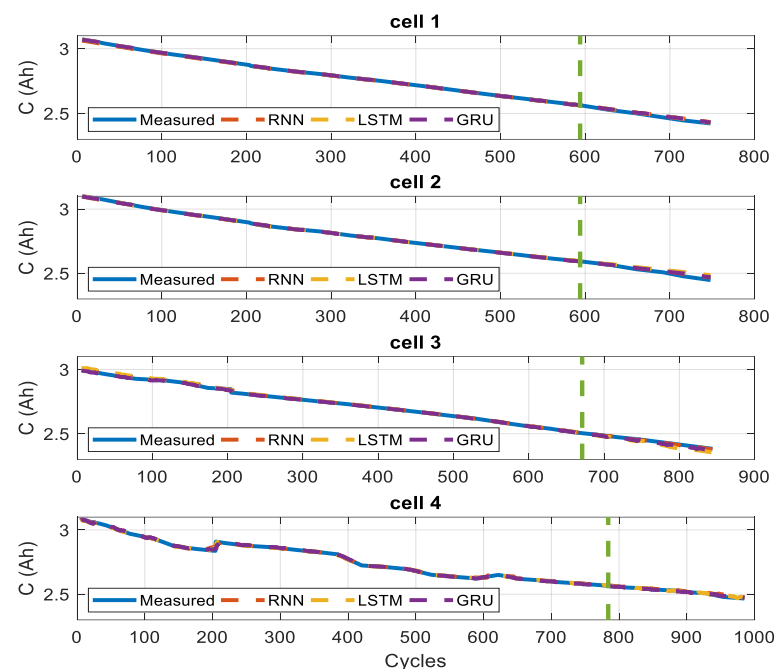


**Figure 11.** Prediction results of the three prognosis models in comparison with the measured capacity when the models are trained with 80% of the cycles.

**Table 4.** Parameters of GRU neural networks.

Prognosis Models	Battery Cells	60% of Cycles		70% of Cycles		80% of Cycles	
		MAPE (%)	RMSE (Ah)	MAPE (%)	RMSE (Ah)	MAPE (%)	RMSE (Ah)
RNN	Cell 1	0.555	0.014	0.486	0.012	0.566	0.014
	Cell 2	0.515	0.013	0.676	0.017	0.809	0.020
	Cell 3	0.560	0.014	0.642	0.016	0.228	0.006
	Cell 4	1.552	0.041	0.279	0.007	0.442	0.012
	Mean	0.795	0.020	0.521	0.013	0.511	0.013
LSTM	Cell 1	2.043	0.050	1.197	0.029	0.509	0.012
	Cell 2	2.171	0.054	0.500	0.013	1.586	0.039
	Cell 3	1.043	0.026	1.071	0.026	0.645	0.016
	Cell 4	1.206	0.032	0.529	0.014	0.187	0.005
	Mean	1.616	0.040	0.824	0.020	0.732	0.018
GRU	Cell 1	1.786	0.044	0.731	0.018	0.572	0.014
	Cell 2	0.644	0.016	0.737	0.018	0.938	0.023
	Cell 3	0.670	0.017	1.000	0.025	0.605	0.015
	Cell 4	1.183	0.031	0.729	0.019	0.169	0.004
	Mean	1.071	0.027	0.799	0.020	0.571	0.014

The comparisons between the prognosis models show that the RNN model presents accurate prediction results for the three training percentage sets: in the case of 60% of training cycles, the mean MAPE error is less than 0.8% for the RNN model, less than 1.1% for the GRU model, and less than 1.62% for the LSTM model. The superiority of the RNN model is related to its simplicity, which allows it to achieve high accuracy even with a small amount of data; however, as the training set increases, we observe that the prediction errors of the LSTM and the GRU decrease and the differences between the prediction errors of the three models decreases. As presented in Table 4, with 80% of training cycles, the GRU and the RNN present the same mean error (about 0.7%), while the LSTM prediction mean error is less than 0.75%.

In order to compare the prediction models in term of complexity, the computational time of the training process is presented in Table 5. The three recurrent networks (RNN, LSTM, and GRU) are developed using a Python library, TensorFlow. The algorithms are trained and tested in the Windows 10® environment. The computer used is equipped with an i-5 processor 2.50 (GHz) and 16 GB of RAM.

**Table 5.** Training time of three prediction models for the three training sets: 60%, 70%, and 80% of the cycles.

Prediction Model	Training Time (s)		
	60%	70%	80%
RNN	32.7	35.1	44.6
LSTM	101.6	128.4	146.6
GRU	38.2	45.0	50.9

The results presented in the Table 5 show, as expected, that increasing the training data leads to increasing the training time for all models. The results obtained are in agreement with the description of the architectures of the prediction models in Section 2.3: the comparison shows that the LSTM neural network has the highest training time (higher

than 100 s) followed by the GRU neural networks with a training time less than 51 s, where the RNN has a training time less than 44.6 s.

Finally, the precision of the prediction of the three prognosis algorithms is compared with the methods proposed in the literature in Table 6. The comparison shows that the simple architectures proposed in this study have prediction accuracies similar to those of other studies that proposed complex and hybrid models for the prognosis of batteries.

**Table 6.** Results comparison with the literature.

Prediction Model	Input Features	Dataset	MAPE
Variational modal decomposition with entropy detection-GRU [44]	Capacity	NASA and CALCE datasets, laboratory tests	<0.64%
CEEDMAN algorithm—CNN-LSTM [21]	Capacity	NASA datasets and laboratory tests	<2%
LSTM with Explainable IA-Optimal features selection [45]	Cycles, Current, Voltage, Temperature	NASA dataset	<2%
Multi-kernel RVM-Particle swarm optimization [46]	Capacity	Laboratory tests	<1.34%
Multi-Layer Perceptron deep neural network [47]	Impedance measurements features	Cavendish Laboratory University of Cambridge	<0.97%
RNN this study			<1.55%
LSTM this study	Cycle number and mean temperature	Experimental tests	<2.17%
GRU this study			<1.78%

#### 4. Conclusions

Lithium-ion battery health prognosis is necessary for an optimal and reliable battery management of an electrical vehicle. This paper compares and evaluates three recurrent neural network models for a multi-step capacity prediction of NMC lithium-ion batteries. These prognosis models allow the prediction of the capacity based on the thermal features of the battery cells. The features are extracted and selected based on the correlation analysis between the experimental data and the battery capacity. The model training and evaluation were performed based on experimental data generated from accelerated ageing tests. During these tests, four NMC cells were cycled using dynamic current profile extracted from the WLTC procedure under a controlled temperature of 35 °C. The predictions were evaluated and compared considering three different percentages of the training sets: 60%, 70% and 80% of the cells cycles. The analysis and comparison of the results show that the GRU model is the most suitable prognosis model for vehicular applications, as it has shown good performance for multi-step prediction and offers a good compromise between prediction accuracy and complexity.

Future work will focus on the extension and the evaluation of the prediction models at different temperatures and state-of-charge cycling windows, in order to generalize their performance to the different working conditions of vehicle batteries.

**Author Contributions:** A.H.: Methodology, Formal analysis, Data curation, Writing original draft preparation. B.T.-I.: Review, Data curation, Investigation, Visualization, Supervision. P.M.: Methodology, Review, Investigation, Visualization, Supervision. H.G.: Methodology, Investigation, Review, Visualization, Supervision. All authors have read and agreed to the published version of the manuscript.

**Funding:** This research received no external funding.

**Data Availability Statement:** The data presented in this study are available on request from the corresponding author. The data are not publicly available due to [the privacy of the laboratory tests conducted].

**Conflicts of Interest:** The authors declare no conflicts of interest.

## References

1. Veza, I.; Syaifuddin, M.; Idris, M.; Herawan, S.G.; Yusuf, A.A.; Fattah, I.M.R. Electric Vehicle (EV) Review: Bibliometric Analysis of Electric Vehicle Trend, Policy, Lithium-Ion Battery, Battery Management, Charging Infrastructure, Smart Charging, and Electric Vehicle-to-Everything (V2X). *Energies* **2024**, *17*, 3786. [[CrossRef](#)]
2. Gong, X.; Xiong, R.; Mi, C.C. Study of the Characteristics of Battery Packs in Electric Vehicles With Parallel-Connected Lithium-Ion Battery Cells. *IEEE Trans. Ind. Appl.* **2014**, *51*, 1872–1879. [[CrossRef](#)]
3. Chaoui, H.; Ibe-Ekeocha, C.C. State of Charge and State of Health Estimation for Lithium Batteries Using Recurrent Neural Networks. *IEEE Trans. Veh. Technol.* **2017**, *66*, 8773–8783. [[CrossRef](#)]
4. Xia, Z.; Abu Qahouq, J.A. State-of-Charge Balancing of Lithium-Ion Batteries With State-of-Health Awareness Capability. *IEEE Trans. Ind. Appl.* **2020**, *57*, 673–684. [[CrossRef](#)]
5. Rahman, T.; Alharbi, T. Exploring Lithium-Ion Battery Degradation: A Concise Review of Critical Factors, Impacts, Data-Driven Degradation Estimation Techniques, and Sustainable Directions for Energy Storage Systems. *Batteries* **2024**, *10*, 220. [[CrossRef](#)]
6. Cai, J.; Zhang, H.; Jin, X. Aging-aware predictive control of PV-battery assets in buildings. *Appl. Energy* **2018**, *236*, 478–488. [[CrossRef](#)]
7. Shan, C.; Chin, C.S.; Mohan, V.; Zhang, C. Review of Various Machine Learning Approaches for Predicting Parameters of Lithium-Ion Batteries in Electric Vehicles. *Batteries* **2024**, *10*, 181. [[CrossRef](#)]
8. Xiong, R.; Pan, Y.; Shen, W.; Li, H.; Sun, F. Lithium-ion battery aging mechanisms and diagnosis method for automotive applications: Recent advances and perspectives. *Renew. Sustain. Energy Rev.* **2020**, *131*, 110048. [[CrossRef](#)]
9. Lipu, M.H.; Hannan, M.; Hussain, A.; Hoque, M.; Ker, P.J.; Saad, M.; Ayob, A. A review of state of health and remaining useful life estimation methods for lithium-ion battery in electric vehicles: Challenges and recommendations. *J. Clean. Prod.* **2018**, *205*, 115–133. [[CrossRef](#)]
10. Zhang, Y.; Li, Y.-F. Prognostics and health management of Lithium-ion battery using deep learning methods: A review. *Renew. Sustain. Energy Rev.* **2022**, *161*, 112282. [[CrossRef](#)]
11. Toughzaoui, Y.; Toosi, S.B.; Chaoui, H.; Louahlia, H.; Petrone, R.; Le Masson, S.; Gualous, H. State of health estimation and remaining useful life assessment of lithium-ion batteries: A comparative study. *J. Energy Storage* **2022**, *51*, 104520. [[CrossRef](#)]
12. El Mejdoubi, A.; Chaoui, H.; Gualous, H.; Bossche, P.V.D.; Omar, N.; Van Mierlo, J. Lithium-Ion Batteries Health Prognosis Considering Aging Conditions. *IEEE Trans. Power Electron.* **2018**, *34*, 6834–6844. [[CrossRef](#)]
13. Hu, X.; Xu, L.; Lin, X.; Pecht, M. Battery Lifetime Prognostics. *Joule* **2020**, *4*, 310–346. [[CrossRef](#)]
14. Ossai, C.I. Prognosis and Remaining Useful Life Estimation of Lithium-Ion Battery with Optimal Multi-Level Particle Filter and Genetic Algorithm. *Batteries* **2018**, *4*, 15. [[CrossRef](#)]
15. Pang, H.; Chen, K.; Geng, Y.; Wu, L.; Wang, F.; Liu, J. Accurate capacity and remaining useful life prediction of lithium-ion batteries based on improved particle swarm optimization and particle filter. *Energy* **2024**, *293*, 130555. [[CrossRef](#)]
16. Lin, Y.-H.; Tian, L.-L.; Ding, Z.-Q. Ensemble Remaining Useful Life Prediction for Lithium-Ion Batteries With the Fusion of Historical and Real-Time Degradation Data. *IEEE Trans. Veh. Technol.* **2023**, *72*, 5934–5947. [[CrossRef](#)]
17. Hu, X.; Che, Y.; Lin, X.; Deng, Z. Health Prognosis for Electric Vehicle Battery Packs: A Data-Driven Approach. *IEEE/ASME Trans. Mechatron.* **2020**, *25*, 2622–2632. [[CrossRef](#)]
18. Li, J.; Peng, Y.; Wang, Q.; Liu, H. Status and Prospects of Research on Lithium-Ion Battery Parameter Identification. *Batteries* **2024**, *10*, 194. [[CrossRef](#)]
19. Sun, C.; Lu, T.; Li, Q.; Liu, Y.; Yang, W.; Xie, J. Predicting the Future Capacity and Remaining Useful Life of Lithium-Ion Batteries Based on Deep Transfer Learning. *Batteries* **2024**, *10*, 303. [[CrossRef](#)]
20. Bellomo, M.; Giazitzis, S.; Badha, S.; Rosetti, F.; Dolara, A.; Ogliari, E. Deep Learning Regression with Sequences of Different Length: An Application for State of Health Trajectory Prediction and Remaining Useful Life Estimation in Lithium-Ion Batteries. *Batteries* **2024**, *10*, 292. [[CrossRef](#)]
21. Jia, Z.; Jia, Z.; Li, Z.; Li, Z.; Zhao, K.; Zhao, K.; Wang, K.; Wang, K.; Wang, S.; Wang, S.; et al. CNN-DBLSTM: A long-term remaining life prediction framework for lithium-ion battery with small number of samples. *J. Energy Storage* **2024**, *97 Pt B*, 112947. [[CrossRef](#)]
22. Al-Wreikat, Y.; Serrano, C.; Sodré, J.R. Driving behaviour and trip condition effects on the energy consumption of an electric vehicle under real-world driving. *Appl. Energy* **2021**, *297*, 117096. [[CrossRef](#)]
23. Chen, X.; Hu, Y.; Li, S.; Wang, Y.; Li, D.; Luo, C.; Xue, X.; Xu, F.; Zhang, Z.; Gong, Z.; et al. State of health (SoH) estimation and degradation modes analysis of pouch NMC532/graphite Li-ion battery. *J. Power Sources* **2021**, *498*, 229884. [[CrossRef](#)]

24. Vespaiboon, S.; Pora, W. Analyzing Computational Complexity and Footprint: A Comparative Study of State of Charge Estimation across Various Equivalent Circuit Models for Batteries. In Proceedings of the 2024 21st International Conference on Electrical Engineering/Electronics, Computer, Telecommunications and Information Technology (ECTI-CON), Khon Kaen, Thailand, 27–30 May 2024; pp. 1–5. [CrossRef]
25. Sadil, J.; Kekula, F.; Majera, J.; Pisharodi, V. Comparison of Capacity Fade for the Constant Current and WLTC Drive Cycle Discharge Modes for Commercial LiFeYPO<sub>4</sub> Cells Used in xEV Vehicles. *Batteries* **2022**, *8*, 282. [CrossRef]
26. Hammou, A.; Petrone, R.; Diallo, D.; Gualous, H. Estimating the Health Status of Li-ion NMC Batteries from Energy Characteristics for EV Applications. *IEEE Trans. Energy Convers.* **2023**, *38*, 2160–2168. [CrossRef]
27. Hammou, A.; Petrone, R.; Gualous, H.; Diallo, D. Deep learning framework for state of health estimation of NMC and LFP Li-ion batteries for vehicular applications. *J. Energy Storage* **2023**, *70*, 108083. [CrossRef]
28. Tian, J.; Fan, Y.; Pan, T.; Zhang, X.; Yin, J.; Zhang, Q. A critical review on inconsistency mechanism, evaluation methods and improvement measures for lithium-ion battery energy storage systems. *Renew. Sustain. Energy Rev.* **2024**, *189 Pt B*, 113978. [CrossRef]
29. Leng, F.; Tan, C.M.; Pecht, M. Effect of Temperature on the Aging rate of Li Ion Battery Operating above Room Temperature. *Sci. Rep.* **2015**, *5*, 12967. [CrossRef] [PubMed]
30. Shen, W.; Wang, N.; Zhang, J.; Wang, F.; Zhang, G. Heat Generation and Degradation Mechanism of Lithium-Ion Batteries during High-Temperature Aging. *ACS Omega* **2022**, *7*, 44733–44742. [CrossRef]
31. Kampik, M.; Bodzek, K.; Piaskowy, A.; Pilśniak, A.; Fice, M. An Analysis of Energy Consumption in Railway Signal Boxes. *Energies* **2023**, *16*, 7985. [CrossRef]
32. Azizighalehsari, S.; Venugopal, P.; Singh, D.P.; Rietveld, G. Performance Evaluation of Retired Lithium-ion Batteries for Echelon Utilization. In Proceedings of the IECON 2022—48th Annual Conference of the IEEE Industrial Electronics Society, Brussels, Belgium, 17–20 October 2022; pp. 1–6. [CrossRef]
33. Hewamalage, H.; Bergmeir, C.; Bandara, K. Recurrent Neural Networks for Time Series Forecasting: Current status and future directions. *Int. J. Forecast.* **2021**, *37*, 388–427. [CrossRef]
34. Runge, J.; Zmeureanu, R. A Review of Deep Learning Techniques for Forecasting Energy Use in Buildings. *Energies* **2021**, *14*, 608. [CrossRef]
35. Chen, Y.; Cheng, Q.; Cheng, Y.; Yang, H.; Yu, H. Applications of recurrent neural networks in environmental factor forecasting: A review. *Neural Comput.* **2018**, *30*, 2855–2881. [CrossRef]
36. Liu, Y.; Wang, X.; Wang, L.; Liu, D. A modified leaky ReLU scheme (MLRS) for topology optimization with multiple materials. *Appl. Math. Comput.* **2019**, *352*, 188–204. [CrossRef]
37. Kingma, D.P.; Ba, J. Adam: A Method for Stochastic Optimization. In Proceedings of the 3rd International Conference on Learning Representations, ICLR, Conference Track Proceedings, Diego, CA, USA, 7–9 May 2015.
38. Hochreiter, S.; Schmidhuber, J. Long Short-Term Memory. *Neural Comput.* **1997**, *9*, 1735–1780. [CrossRef] [PubMed]
39. Cho, K.; Van Merriënboer, B.; Bahdanau, D.; Bengio, Y. On the properties of neural machine translation: Encoder-decoder approaches. *arXiv* **2014**, arXiv:1409.1259. [CrossRef]
40. He, K.; Zhang, X.; Ren, S.; Sun, J. Delving deep into rectifiers: Surpassing human-level performance on imagenet classification. In Proceedings of the IEEE International Conference on Computer Vision, Las Condes, Chile, 11–18 December 2015; pp. 1026–1034.
41. Safavi, V.; Vaniar, A.M.; Bazmohammadi, N.; Vasquez, J.C.; Keysan, O.; Guerrero, J.M. Early prediction of battery remaining useful life using CNN-XGBoost model and Coati optimization algorithm. *J. Energy Storage* **2024**, *98 Pt B*, 113176. [CrossRef]
42. Jadon, A.; Patil, A.; Jadon, S. A Comprehensive Survey of Regression-Based Loss Functions for Time Series Forecasting. In *Data Management, Analytics and Innovation. ICDMAI 2024. Lecture Notes in Networks and Systems*; Sharma, N., Goje, A.C., Chakrabarti, A., Bruckstein, A.M., Eds.; Springer: Singapore, 2024; Volume 998. [CrossRef]
43. Chen, X.; Yang, L.; Xue, H.; Li, L.; Yu, Y. A Machine Learning Model Based on GRU and LSTM to Predict the Environmental Parameters in a Layer House, Taking CO<sub>2</sub> Concentration as an Example. *Sensors* **2024**, *24*, 244. [CrossRef]
44. Liu, H.; Li, Y.; Luo, L.; Zhang, C. A Lithium-Ion Battery Capacity and RUL Prediction Fusion Method Based on Decomposition Strategy and GRU. *Batteries* **2023**, *9*, 323. [CrossRef]
45. Vakharia, V.; Shah, M.; Nair, P.; Borade, H.; Sahlot, P.; Wankhede, V. Estimation of Lithium-ion Battery Discharge Capacity by Integrating Optimized Explainable-AI and Stacked LSTM Model. *Batteries* **2023**, *9*, 125. [CrossRef]
46. Jiang, B.; Dai, H.; Wei, X.; Jiang, Z. Multi-Kernel Relevance Vector Machine With Parameter Optimization for Cycling Aging Prediction of Lithium-Ion Batteries. *IEEE J. Emerg. Sel. Top. Power Electron.* **2021**, *11*, 175–186. [CrossRef]
47. Bao, M.; Liu, D.; Wu, Y.; Wang, Z.; Yang, J.; Lan, L.; Ru, Q. Interpretable machine learning prediction for li-ion battery's state of health based on electrochemical impedance spectroscopy and temporal features. *Electrochim. Acta* **2024**, *494*, 144449. [CrossRef]

**Disclaimer/Publisher’s Note:** The statements, opinions and data contained in all publications are solely those of the individual author(s) and contributor(s) and not of MDPI and/or the editor(s). MDPI and/or the editor(s) disclaim responsibility for any injury to people or property resulting from any ideas, methods, instructions or products referred to in the content.